Kompositkristalls und ermöglicht es, ohne weiteres einen Abstand zwischen zwei Atomen verschiedener Teilsysteme, deren Koordinaten gleiche **t**-Komponenten aufweisen, zu berechnen.

Alle im vorhergehenden erwähnten Rechenprogramme außer *SPCCC* sind bereits als *Supplementary Publication* zu den kurzen Veröffentlichungen (Kato & Onoda, 1991*a*,*b*, 1992) hinterlegt worden. Ihre revidierte Fassung* sowie das neue Programm* sind direkt bei dem Verfasser erhältlich.

Frau Dr M. Onoda danke ich für die Anregung zu dieser Veröffentlichung.

* Die Quelltexte und Beschreibungen der Programme sind bei dem British Library Document Supply Centre (Supplementary Publication No. SUP 71689: 124 pp.) hinterlegt. Kopien sind erhältlich durch: The Managing Editor, International Union of Crystallography, 5 Abbey Square, Chester CH1 2HU, England.

Literatur

GUEMAS, L., RABU, P., MEERSCHAUT, A. & ROUXEL, J. (1988). *Mater. Res. Bull.* **23**, 1061–1069.

JANNER, A. & JANSSEN, T. (1980*a*). *Acta Cryst.* A**36**, 399–408.

JANNER, A. & JANSSEN, T. (1980*b*). *Acta Cryst.* A**36**, 408–415.

KATO, K. (1990). *Acta Cryst.* B**46**, 39–44.

KATO, K. & ONODA, M. (1991*a*). *Acta Cryst.* A**47**, 55–56.

KATO, K. & ONODA, M. (1991*b*). *Acta Cryst.* A**47**, 448–449.

KATO, K. & ONODA, M. (1992). *Acta Cryst.* A**48**, 73–76.

KATO, K., TAKAYAMA-MUROMACHI, E., KOSUDA, K. & UCHIDA, Y. (1988). *Acta Cryst.* C**44**, 1881–1884.

MCCARRON, E. M. III, SUBRAMANIAN, M. A., CALABRESE, J. C. & HARLOW, R. L. (1988). *Mater. Res. Bull.* **23**, 1355–1365.

MEETSMA, A., WIEGERS, G. A., HAANGE, R. J. & DE BOER, J. L. (1989). *Acta Cryst.* A**45**, 285–291.

ONODA, M. & KATO, K. (1991). *Acta Cryst.* B**47**, 630–634.

ONODA, M., KATO, K., GOTOH, Y. & OOSAWA, Y. (1990). *Acta Cryst.* B**46**, 487–492.

ONODA, M., SAEKI, M., YAMAMOTO, A. & KATO, K. (1993). *Acta Cryst.* B**49**, 929–936.

OOSAWA, Y., GOTOH, Y. & ONODA, M. (1989). *Chem. Lett. S.* 523–524.

SIEGRIST, T., SCHNEEMEYER, L. F., SUNSHINE, S. A., WASZCZAK, J. V. & ROTH, R. S. (1988). *Mater. Res. Bull.* **23**, 1429–1438.

WIEGERS, G. A., MEETSMA, A., HAANGE, R. J. & DE BOER, J. L. (1988). *Mater. Res. Bull.* **23**, 1551–1559.

WIEGERS, G. A., MEETSMA, A., HAANGE, R. J. & DE BOER, J. L. (1989). *Solid State Ionics*, **32/33**, 183–191.

WIEGERS, G. A., MEETSMA, A., VAN SMAALEN, S., HAANGE, R. J., WULFF, J., ZEINSTRA, T., DE BOER, J. L., KUYPERS, S., VAN TENDELOO, G., VAN LANDUYT, J., AMELINCKX, S., MEERSCHAUT, A., RABU, P. & ROUXEL, J. (1989). *Solid State Commun.* **70**, 409–413.

WILLIAMS, T. B. & HYDE, B. G. (1988). *Acta Cryst.* B**44**, 467–474.

YAMAMOTO, A. (1982). *Acta Cryst.* A**38**, 87–92.

YAMAMOTO, A. (1993). *Acta Cryst.* A**49**, 831–846.

Acta Cryst. (1994). A**50**, 357–366

Smooth Parabolas in Transmission Electron Diffraction Patterns

BY R. JAMES, D. M. BIRD AND A. G. WRIGHT*

School of Physics, University of Bath, Bath BA2 7AY, England

(*Received* 6 *July* 1993; *accepted* 19 *November* 1993)

Abstract

Perturbation theory is used to analyse the geometry of various diffracted features in large-angle high-energy electron diffraction patterns taken in transmission. Particular attention is paid to smooth parabolic features and their straight-line envelopes. It is shown that the features lie in positions determined by a 'modified Bragg condition' that takes account of dynamical interactions in the crystal. The results have considerable bearing on the interpretation of almost identical resonance features seen in reflection high-energy electron diffraction.

* Now at Department of Chemical Engineering and Materials Science, University of Minnesota, Minneapolis, Minnesota, USA.

1. Introduction

In this paper, features are analysed that may be seen in just about any 'near-axis' convergent-beam high-energy electron diffraction (HEED) pattern. Of most interest are smooth parabolas (smoother for strongly scattering materials such as platinum than for weaker scatterers such as GaAs; these materials are used as examples) and the straighter lines that surround them. Our particular aim is to account for the positions and shapes of the features as functions of material and zone axis. A distorted-wave Born expansion is sufficient to yield our result, which is couched in terms of a Bragg condition modified to include the effect of dynamical scattering of the incident electrons. Much of the argument may

equally be based upon the notions of conservation of energy and momentum in the diffraction process. This is an important point, as our subsidiary aim is to pave the way for an explanation of very similar 'resonance' features seen in off-axis convergent-beam reflection HEED (CB-RHEED) patterns (James, Bird & Wright, 1994).

The first detailed observation that the parabolic features seen in RHEED are present in transmission patterns was made by Lehmpfuhl & Dowell (1986), for the rather weak silicon (111) surface. [Since RHEED patterns are usually taken at glancing angles to a zone axis lying in the plane of the surface, the equivalent region in which to look for similar features in transmission HEED (THEED) is tilted off the same axis, in the same 'surface-normal' direction.] Similar observations have been reported by the Arizona group, notably by Peng, Cowley & Yao (1988) and Yao & Cowley (1989). One common feature of these papers is that the THEED patterns shown are all off-axis Kossel–Möllenstedt patterns. Although the features of interest are certainly visible in such patterns (and in just about any other pattern taken at the correct orientation), the geometry is not nearly so clear as in bright-field large-angle convergent-beam electron diffraction (LACBED) patterns, as introduced by Tanaka, Saito, Ueno & Harada (1980). These patterns are produced by over- (or under-) focusing a large-angle incident probe and using the selected-area aperture to pick out the zeroth beam at a position where the (otherwise overlapping) discs are separated. The drawback of the overfocusing is that a large flat area of the specimen is required, perhaps thousands of ångströms in diameter. However, the additional feature of the patterns, that both image and diffraction information are present, makes the search for an acceptable area and the interpretation of distortions incurred somewhat easier.

Fig. 1 shows 200 kV bright-field LACBED patterns taken from close to the Pt[231] and GaAs[116] axes. Note that the directions from the left to the right of these patterns are $[1\bar{1}1]$ and $[1\bar{1}0]$, respectively; the vertical deficiency lines are therefore $(n\bar{n}n)$ and $(n\bar{n}0)$. These are the least interesting features in the patterns but do serve as useful landmarks. The similarities between these patterns and CB-RHEED patterns at similar orientations have been highlighted in a brief report by James, Bird & Wright (1989).

The rest of the paper is built around the patterns in Fig. 1. In §2, a numerical simulation is used to establish that straightforward dynamical diffraction theory is sufficient to produce the lines of interest in the correct places and to provide 'idealized experimental data' for comparison with the approximate theory presented in §3. The reason for moving to an approximation method is to extract *analytical* expressions for the conditions necessary to produce the smooth parabolas and their envelopes. The numerical simulations may then be used to determine what, if anything, has been lost in making the approximations. The results of the perturbation theory, which give an unequivocal explanation of the geometry of the patterns, are presented in §4 and discussed in §5, with particular reference to what they might tell us about the RHEED case.

We now run quickly through the fundamentals of dynamical theory in order to set up the equations that are used later and to introduce our notation. We make the forward scattering and projection approximations to separate out the very different longitudinal (z) and transverse $\mathbf{R} = (x,y)$ behaviours of the incident electrons. The basic equation governing the fast-electron wavefunction Φ as a function of $\mathbf{r} = (\mathbf{R},z)$ is then (*e.g.* Howie, 1966; Berry, 1971; Bird,

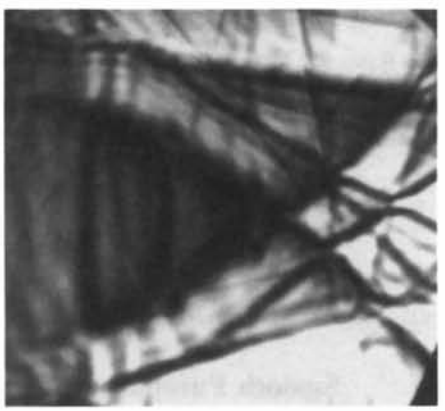

(*a*)

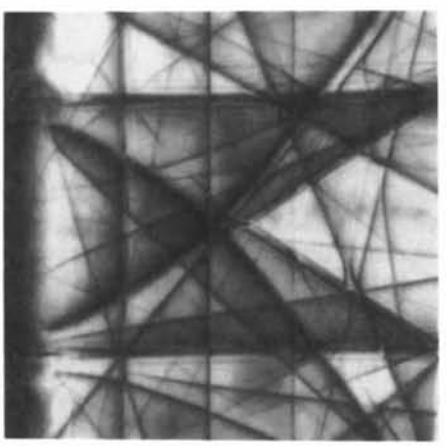

(*b*)

Fig. 1. 200 kV bright-field LACBED patterns taken close to (*a*) the Pt[231] zone axis and (*b*) the GaAs[116] zone axis. In both cases, the zone axis is situated off the left edge of the figure, half-way up.

1989)

$$[-\nabla_{\mathbf{R}}^2 + U(\mathbf{R})]\Phi(\mathbf{r}) = 2ik\partial\Phi/\partial z\,, \qquad (1)$$

where k is the magnitude of the incident electron wave vector. z is the direction of projection and the direction of the zone axis off which we tilt; the crystal is assumed to be flat and parallel sided, lying in the $\mathbf{R}$ plane perpendicular to z. Equation (1) is exactly analogous to the time-dependent Schrödinger equation, with $\mathbf{R}$ the spatial coordinate and z taking the place of time – this similarity is exploited in the perturbation theory of §3. $U(\mathbf{R})$ is the effective two-dimensional 'potential', which is related to the actual projected potential $V(\mathbf{R})$ by

$$U(\mathbf{R}) = (2\gamma m_0/\hbar^2)V(\mathbf{R}) = \sum_{\mathbf{G}} U_{\mathbf{G}} \exp(i\mathbf{G}\cdot\mathbf{R}). \qquad (2)$$

We have expressed the periodic potential as a sum over Fourier coefficients, $U_{\mathbf{G}}$, where the $\mathbf{G}$ represent the two-dimensional set of zero-layer reciprocal-lattice vectors. The solutions to (1) are separable in $\mathbf{R}$ and z and can be expressed in the form of Bloch waves, $\Phi^{(j)}$, each of which has an excitation amplitude $\varepsilon^{(j)}$;

$$\Phi^{(j)} = \sum_{\mathbf{G}} C_{\mathbf{G}}^{(j)}(\mathbf{K}) \exp[i(\mathbf{K}+\mathbf{G})\cdot\mathbf{R}] \exp[-is^{(j)}(\mathbf{K})z/2k] \qquad (3a)$$

$$\Phi = \sum_j \varepsilon^{(j)}\Phi^{(j)}. \qquad (3b)$$

The Bloch-wave coefficients $C_{\mathbf{G}}^{(j)}$ and transverse energies $s^{(j)}$ are the eigenvectors and eigenvalues, respectively, of the many-beam equations

$$\sum_{\mathbf{G}'}\{[(\mathbf{K}+\mathbf{G})^2 - s^{(j)}]\delta_{\mathbf{G},\mathbf{G}'} + U_{\mathbf{G}-\mathbf{G}'}\}C_{\mathbf{G}'}^{(j)} = 0, \qquad (4)$$

where $\mathbf{K}$ is chosen to match the component of the incident wave vector parallel to the specimen surfaces. Finally, the boundary condition at the entrance surface, $z=0$, is satisfied by setting $\varepsilon^{(j)} = C_{\mathbf{0}}^{(j)*}$. Note that we ignore absorption, as we are only interested in the *positions* of the features, not their relative intensities. Although there are higher-order Laue-zone (HOLZ) deficiency lines in Fig. 1, they are not of interest here and are neglected in our theory.

2. Numerical simulation of LACBED patterns

As always when approximations are used, it is useful to have a reliable more exact theory with which to compare results. We therefore simulate the patterns of Fig. 1 by solving the many-beam equations (4). The diffracted amplitudes at the exit face of a perfect transmission specimen in the symmetric Laue geometry, as a function of the two-dimensional orientation $\mathbf{K}$, are given by

$$A_{\mathbf{G}}(\mathbf{K},t) = \sum C_{\mathbf{0}}^{(j)*}(\mathbf{K})C_{\mathbf{G}}^{(j)}(\mathbf{K}) \exp(-is^{(j)}t/2k), \qquad (5)$$

where t is the specimen thickness. Since in a bright-field pattern only the component $\mathbf{G}=\mathbf{0}$ is of interest, the diffracted intensity at any orientation $\mathbf{K}$ is

$$I_{\mathbf{0}}(t) = \left|\sum_j |C_{\mathbf{0}}^{(j)}|^2 \exp(-is^{(j)}t/2k)\right|^2$$
$$= \sum_{i,j} |C_{\mathbf{0}}^{(i)}C_{\mathbf{0}}^{(j)}|^2 \cos[(s^{(i)} - s^{(j)})(t/2k)]. \qquad (6)$$

The cosine term in the second of these expressions is an interference term and is responsible for the fringes seen parallel to and either side of the main diffraction lines. For the purposes of finding only the positions of these main lines, the time-consuming double summation is unnecessary. We set $i=j$ so

$$I_{\mathbf{0}}(\mathbf{K}) \simeq \sum_j |C_{\mathbf{0}}^{(j)}(\mathbf{K})|^4, \qquad (7)$$

independent of the specimen thickness. Fig. 2 shows simulated LACBED bright-field intensities, using (7), for the same materials and regions as the experimen-

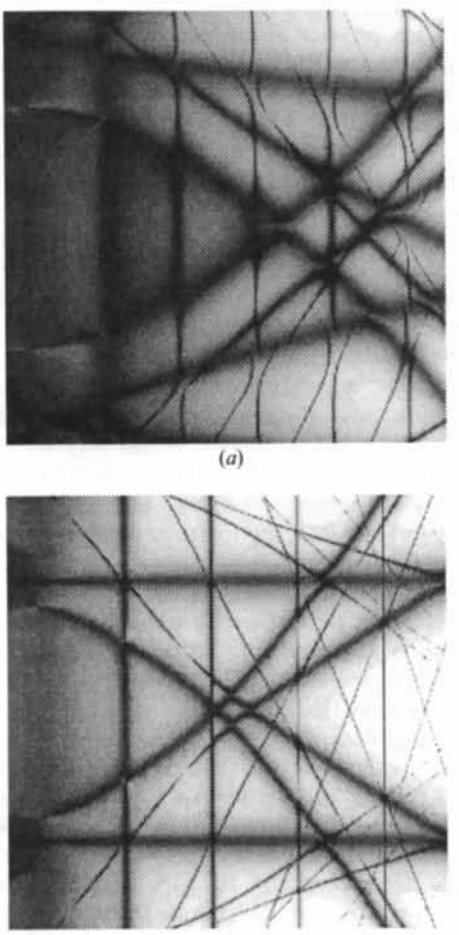

(*a*)

(*b*)

Fig. 2. Simulated bright-field intensities close to (*a*) the Pt[231] zone axis and (*b*) the GaAs[116] zone axis at 200 kV. See text for details.

tal patterns of Fig. 1. In both cases, the orientation scan is for $-4 \le K_y \le 4$ Å^{-1} vertically and $1 \le K_x \le 9$ Å^{-1} horizontally. As a guide to the area of the reciprocal lattice covered by these scans, $G_{111} = 2.77$ Å^{-1} in platinum and $G_{220} = 3.15$ Å^{-1} in GaAs. About 40 or 50 beams are included in the many-beam expansion. In both simulations, the intensity is scaled to cover the range [0, 1] to highlight the contrast between the deficit lines of interest and the background. There is clear agreement between experiment and computed simulation in terms of the *positions* of the major features, which we emphasize again are the sole concern of this paper. Having achieved this agreement, we now have a 'perfect experiment' with which to compare the approximations that follow. (Note that we can tell which lines in the experiment are HOLZ lines by comparison of Figs. 1 and 2.)

3. A perturbative 'two-rod' theory in transmission

Much of the physics of surface resonance associated with parabolas in RHEED patterns can be extracted using two-rod theory (*e.g.* McRae, 1979). The 'rods' are the result of loss of symmetry in the direction normal to the surface. If it is assumed that the RHEED electrons do not penetrate the bulk of the specimen, these rods are totally featureless along their length. The much-discussed phenomenon of surface resonance is then associated with inter-rod scattering from the zeroth rod into a bound state of some other rod (*e.g.* Marten & Meyer-Ehmsen, 1985; Bird, 1987).

Essentially, we mimic two-rod theory for the transmission case. It should be stressed immediately, however, that what follows is in no way an analysis of RHEED itself, which is by its nature a rather different scattering problem to THEED. For instance, in RHEED, the features of interest are seen when electrons are scattered *out of* states travelling parallel, or nearly parallel, to the surface; in bright-field LACBED patterns, the deficiency lines occur when flux is removed *into* some other state. Nonetheless, we do believe that the geometrical interpretation of the LACBED patterns will be of use in the RHEED problem.

The equivalent of the rod is a systematic row, which in Figs. 1 and 2 runs horizontally. We choose to call this the x direction (and the K_x direction, since we assume cubic symmetry), so the y direction (and K_y) runs from bottom to top. Unlike a rod, a systematic row is *not* continuous in reciprocal space, since there must be conservation of crystal momentum in the K_x direction; the rows simply consist of linear sets of reciprocal-lattice points (Fig. 3). As in RHEED two-rod theory, the basis states for expansion are the states of the zeroth row potential and the coupling between rows is treated as a perturbation. This rather artificial separation into scattering along the rows, which may be strong, and scattering between the rows, which is assumed to be weak, clearly ignores the dynamical effects of other sets of systematic rows. Such effects are minimized by choosing zone axes where the 'surface' systematic rows give the strongest diffraction and are further reduced by the fact that the patterns are tilted up the systematic row of interest, so it is unlikely that a significant portion of any other ZOLZ row will be excited. This tilting provides the analogue of the glancing-angle incidence required in reflection diffraction. The formation of a bright-field LACBED pattern may then be depicted in terms of an incident plane wave with large $K^2 = K_x^2 + K_y^2$ (since we are at comparatively large angles from the zone axis, $\mathbf{K} = \mathbf{0}$), being scattered into and out of other systematic row states.

As the potential is to be split into systematic row contributions, it is convenient to write the starting diffraction equation, (1), as

$$[-\nabla_{\mathbf{R}}^2 + U_0(x) + U(x,y)]\Phi(x,y,z) = 2ik\partial\Phi/\partial z\,, \quad (8)$$

where $-\nabla_{\mathbf{R}}^2 + U_0(x)$ is the unperturbed Hamiltonian. This goes further than the original projection approximation in splitting the problem into x, y and z components. The eigenstates of the unperturbed Hamiltonian are Φ_0 and the perturbation is

$$U(x,y) = \sum_{G_y \neq 0} U_{G_y}(x) \exp(iG_y y), \quad (9a)$$

where

$$U_{G_y}(x) = (1/b)\int_0^b \mathrm{d}y\, U(x,y) \exp(-iG_y y). \quad (9b)$$

b is the crystal repeat unit in the y direction. Note that, since $U(x,y)$ is already projected in z, the

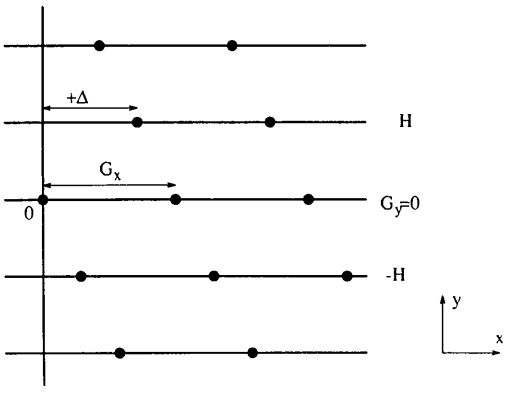

Fig. 3. Schematic showing and defining the sense of the offset Δ between reciprocal-lattice systematic rows. The black dots are individual reciprocal-lattice points.

potential $U_0(x)$ in (9*a*) is the full scattering potential projected in both y and z. $U_0(x)$ therefore depends only on x, so (8) is now separable into x, y and z components, rather than just **R** and z. We may then write $\Phi_0 = \Psi(x)Y(y)Z(z)$. The z dependence is already taken care of in (1) and we now assume that the y dependence, giving inter-row scattering, is weak and well described as a plane wave. Thus,

$$Z(z) = \exp(-is^{(j)}z/2k); \quad Y(y) = \exp(iK_y y). \tag{10}$$

The $\Psi(x)$ are Bloch states of the one-dimensional zeroth systematic row, satisfying

$$\left[-\frac{d^2}{dx^2} + U_0(x)\right]\Psi^{(j)}(x,K_x) = \sigma^{(j)}(K_x)\Psi^{(j)}(x,K_x), \tag{11}$$

where the one-dimensional energy eigenvalues $\sigma^{(j)}$ of $\Psi^{(j)}$ are related to the two-dimensional eigenvalues $s^{(j)}$ of $\Phi^{(j)}$, defined by (3*a*), *via*

$$s^{(j)}(K_x,K_y) = \sigma^{(j)}(K_x) + K_y^2, \tag{12}$$

since the eigenvalue of $Y(y)$ is K_y^2. Denoting the excitation amplitude of each one-dimensional Bloch state by $\varepsilon^{(j)}(K_x)$, the unperturbed eigenstates are

$$\Phi_0 = \sum_j \varepsilon^{(j)}(K_x)\Psi^{(j)}(x,K_x)\exp(iK_y y) \times \exp[-(iz/2k)(\sigma^{(j)} + K_y^2)]. \tag{13}$$

These states of the zeroth row are responsible for the 'surface parallel' Bragg lines running horizontally across the patterns. As we are interested in large angles of incidence, the incident state (j) can be taken, to a first approximation, to have a plane-wave x dependence, with $\sigma^{(j)} = K_x^2$. Φ_0 is then entirely plane-wave-like. In general, the states into which the incident electrons couple will *not* have a plane-wave x dependence.

The basis states Φ_0 may now be perturbed by the potential $U(x,y)$, which will transform K_y by a G_y and cause intra-row scattering between branches (j) with an amplitude that must be depth dependent. This analysis is entirely analogous to that of the time-dependent perturbation theory of the Schrödinger equation – see, for example, Schiff (1968). The perturbed wave function is therefore

$$\Phi = \sum_{j,G_y} a_{j,G_y}(z)\Psi^{(j)}\exp[i(K_y + G_y)y] \times \exp\{-(iz/2k)[\sigma^{(j)} + (K_y + G_y)^2]\} \tag{14}$$

with boundary conditions $a_{j,G_y}(0) = \varepsilon^{(j)}\delta_{0,G_y}$ determined by comparison of (13) and (14). Note that, if the projected reciprocal lattice around the axis of interest is not rectangular, then a perpendicular transition between rods will not satisfy conservation of crystal momentum $K_x \rightarrow K_x + G_x$. In this case, the eigenvalue on rows $G_y = \pm H$ into which electrons couple is related to the eigenvalue on rod 0 *via*

$$\sigma^{(j)}_{\pm H} = \sigma^{(j)}_0(K_x \mp \Delta), \tag{15}$$

where Δ is the offset between rods 0 and H, as defined in Fig. 3. The inclusion of this offset is largely a matter of book-keeping; since it only lengthens the equations yet further, it will be omitted until needed. Note that such an offset applies to the labelling of eigenstates as well as eigenvalues.

The wavefunction (14) may now be substituted into the starting equation (8). We multiply to the left by an orthogonal wave function $\Psi^{(j')*}(x)\exp[-i(K_y + G_y')]$ and integrate over a projected unit cell to yield

$$\frac{da_{j,G_y}}{dz} = \frac{1}{2ik}\sum_j \sum_{G_y' \neq G_y} a_{j',G_y'}\langle\Psi^{(j)}|U_{G_y - G_y'}|\Psi^{(j')}\rangle_x \times \exp\{(iz/2k)[\sigma^{(j)} - \sigma^{(j')} + (K_y + G_y)^2 - (K_y + G_y')^2]\}. \tag{16}$$

The x-dependent matrix element in this equation contains most of the physics of the problem; it is this term that governs the strength of inter-row transitions and from which K_x conservation arises [expressed in (15)]. Although the states $\Psi^{(j)}$ and $\Psi^{(j')}$ will both be Bloch states of the *zeroth*-row potential, the matrix element may be thought of as describing the transfer of flux from a Bloch state on one row to a different state on another row $G_y - G_y'$ away, with a strength given by the inter-row potential $U_{G_y - G_y'}$. In order to explain the geometry of Figs. 1 and 2, only 0 and H need be included as possible values of G_y and G_y'. To keep the size of the equations manageable, it is convenient to write

$$\sigma^{(j)} - \sigma^{(j')} - 2K_y H - H^2 = \Omega^{jj'}, \tag{17}$$

though care must be taken to ensure that the ordering of the labels (j) and (j') is kept absolutely consistent. The resulting two-row equations are

$$\frac{da_{j,0}}{dz} = \frac{1}{2ik}\sum_{j'} a_{j',H}\langle\Psi^{(j)}|U_{-H}|\Psi^{(j')}\rangle_x \exp\left(i\frac{\Omega^{jj'}z}{2k}\right) \tag{18a}$$

and

$$\frac{da_{j',H}}{dz} = \frac{1}{2ik}\sum_j a_{j,0}\langle\Psi^{(j')}|U_H|\Psi^{(j)}\rangle_x \exp\left(-i\frac{\Omega^{jj'}z}{2k}\right). \tag{18b}$$

These are exact 'two-rod' equations for the transmission case. The amplitude coefficients a may be split up into orders $a^{(n)}$ in precisely the same way as for normal time-dependent perturbation theory. The zeroth-order terms are the initial confitions, $a^{(0)}_{j,G_y}(0) = \varepsilon^{(j)}\delta_{0,G_y}$. Since there is no incident excitation onto row H (incident electrons are not diffracted until they hit the crystal), the first-order term on row 0 is

zero. Thus, to see any intensity change in the bright field, we must find the second-order terms. [This is nothing new. The same point has been made many times before; kinematic diffraction theory and HOLZ theory (*e.g.* Bird, 1989) are but two examples.] They are

$$a_{j,0}^{(2)}(t) = \sum_{j'j''} \varepsilon^{(j'')} \langle \Psi^{(j)} | U_{-H} | \Psi^{(j')} \rangle_x \langle \Psi^{(j')} | U_H | \Psi^{(j'')} \rangle_x \times (1/\Omega^{j''j'}) \left((1/\Omega^{jj'}) [\exp(i\Omega^{jj'}t/2k) - 1] - \frac{1}{\sigma^{(j)} - \sigma^{(j'')}} \left\{ \exp\left[\frac{i(\sigma^{(j)} - \sigma^{(j'')})t}{2k} \right] - 1 \right\} \right). \quad (19)$$

This expression has a simple physical interpretation. We start with incident electrons in some state (j'') on row 0; scatter *via* the potential U_H into a state (j') on row H and back *via* U_{-H} to state (j) on row 0. The magnitude of the scattered amplitude is basically determined by the incident excitation $\varepsilon^{(j'')}$ and the two matrix elements. The rest of the expression is a shape function, familiar in all diffraction theory; it determines the positions of diffracted features, their subsidiary fringes and so on. $a_{j,0}^{(2)}$ represents the first term in the perturbation expansion that removes flux from the bright-field beam. The loss is maximized along the loci of deficiency lines; this occurs for $j = j''$ (that is, the electrons return to the same state they started in) and $\Omega^{jj'} = 0$. Since the terms in $\Omega^{jj'}$ are not necessarily plane-wave-like, the condition $\Omega^{jj'} = 0$, which is the crux of our geometrical interpretation of these patterns, is not a simple Bragg condition. Instead, it is a *modified* Bragg condition, in which the one-dimensional Bloch-state eigenvalues σ play an important rôle.

4. Branch-by-branch simulation of LACBED patterns

By analogy with the usual (plane-wave) Bragg condition, we deduce that the geometry of off-axis LACBED patterns can be found by mapping out the loci of the orientations (K_x, K_y) that satisfy the modified Bragg condition $\Omega^{jj'} = 0$. This may be achieved directly and simply by assuming the starting (and hence finishing) state to be the plane wave $\Psi^{(j)} = \exp(iK_x x)$, with eigenvalue $\sigma^{(j)} = K_x^2$. As already mentioned, this assumption is valid because the angle of incidence (measured from the zone axis) is comparatively large – coupling may still occur into strongly diffracting states on row H. Note that, with the initial state chosen to be a plane wave, the vertical Bragg lines corresponding to the systematic row reflections G_x will not be simulated. These would only appear if the state $\Psi^{(j)}$ were expressed as the sum of at least two plane waves.

The equations to be solved for the line positions (K_x, K_y) in this case, then, may be found by setting (17) to zero (the exact modified Bragg condition) and reintroducing (15). To produce the two parabolas in each pattern, rows $+H$ and $-H$ must both be used, so

$$K_x^2 \mp 2K_y H - H^2 - \sigma^{(j')}(K_x \mp \Delta) = 0. \quad (20)$$

This equation bears a striking resemblance to the expressions derived for the resonance parabolas in RHEED [especially those by Bird (1987)], apart from some rather important physical considerations. In transmission, K_x is a good quantum number for the eigenvalues $\sigma^{(j')}$; there is a shift Δ between neighbouring rod potentials (unnecessary in RHEED if the rods are truly featureless) and there is no need to include a mean inner potential, $\overline{U}$. The latter must be included in any RHEED calculation since, unlike in the symmetric Laue transmission case, the path-length through the crystal is not even approximately the same for each electron.

The most illuminating type of LACBED pattern to simulate is one taken from the surface of a strong scatterer (since the features to be discussed are then both prominent and distinct) and one in which the offset Δ is nonzero. Both requirements are satisfied by the Pt[231] pattern in Fig. 1. The reason for choosing such a pole is that, with $\Delta = 0$, (20) must necessarily produce a pattern with mirror symmetry about $K_y = 0$. The only way to avoid the effects of Δ for an asymmetric pole is to have no variation of the energy $\sigma^{(j')}$ with K_x. This may be achieved in THEED only by coupling into a completely flat band of the one-dimensional dispersion curve, because of the requirements of momentum conservation. In other words, the degree of mirror symmetry about $K_y = 0$ is a measure of momentum conservation.

Fig. 4 shows the first seven branches of the dispersion surface of the Pt($1\bar{1}1$) systematic row, from an eleven-beam numerical calculation. The number of beams used is consistent with the number used in the two-dimensional LACBED simulations of §2. The most notable feature of this figure is that the first branch is extremely flat and well split off from the other branches. Note the use of symbols to distinguish each branch – the same symbols denote the same j' label throughout the rest of the paper. The values of $\sigma^{(j')}(K_x)$ from this calculation may be inserted numerically and branch by branch into (20), which is then solved for K_y as a function of K_x, using the appropriate value of H for the particular pole. The loci (K_x, K_y) satisfying (20) are plotted in Fig. 5 for the same region close to the Pt[231] pole as simulated before. Apart from the expected absence of the 'surface-parallel' ($n\bar{n}n$)-type lines, these simulations bear a strong resemblance to both the experimental and theoretical patterns of Figs. 1 and 2.

Each line in Fig. 5 is in exactly the same position as in the full dynamical simulation of Fig. 2. The conclusion to be drawn here is clearly that, for a strong scatterer such as platinum, the LACBED diffraction geometry may be understood in terms of a perturbative two-row branch-by-branch analysis.

In particular, it is concluded that the inner smooth parabolas may be generated entirely from branch-1 contributions; note that this is the only flat band and the resulting parabolas are the *only* features that are smooth and symmetrical about $K_y=0$. In addition, the envelope of the parabolas is seen to be a product of branch 2. This is also a strongly dynamical branch in the Pt(1$\bar{1}$1) systematic row. It cannot, therefore, be assumed that such envelopes are normal Kikuchi lines, mapping plane-wave Bragg conditions. Instead, the envelopes are the loci of orientations satisfying the *dynamically modified* Bragg condition for branch 2. The higher branches become progressively weaker, displaying approximately parabolic dispersion and giving rise to straight lines in the diffraction pattern at normal Bragg positions. Such features can only arise in any diffraction pattern if the real-space potential is periodic, in which case the reciprocal space is periodic and K_x must be conserved to within a G_x.

How do these arguments become changed for weaker scatterers? Fig. 6 shows the first seven branches of the GaAs(2$\bar{2}$0) systematic row dispersion curve, and the corresponding [116] branch-by-branch simulation. The symbols again have the same meaning as for the platinum case. It is clear here that, since the first branch is not quite flat, the inner curve is not quite parabolic and that, apart from the

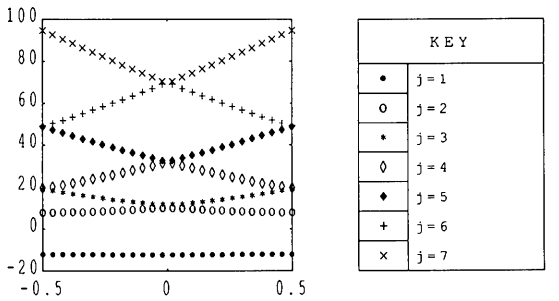

Fig. 4. The first seven branches of the dispersion surface of the Pt(1$\bar{1}$1) systematic row at 200 kV. The vertical axis shows the one-dimensional energy σ, measured in $Å^{-2}$ relative to the mean inner potential. The horizontal axis shows K_x in units of G_x.

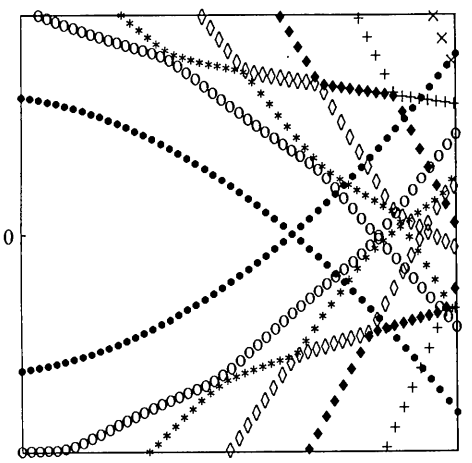

Fig. 5. Branch-by-branch simulation of the 200 kV Pt[231] LACBED pattern of Fig. 1(*a*) using two-row theory. Each line is labelled with the same symbol as the branch of the dispersion surface in Fig. 4 that produces it.

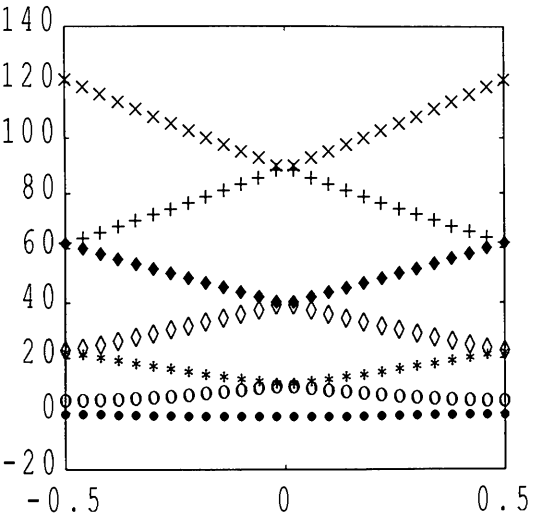

(*a*)

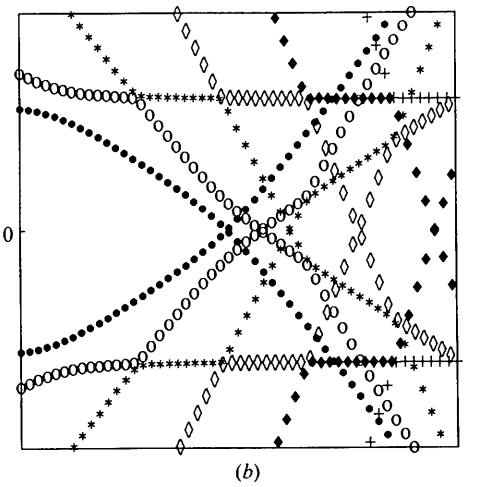

(*b*)

Fig. 6. (*a*) GaAs(2$\bar{2}$0) systematic row dispersion surface at 200 kV. The axes are the same as for the platinum case. (*b*) Branch-by-branch simulation of the GaAs[116] LACBED pattern of Fig. 1(*b*) using (*a*).

dynamical rearrangement of branches 1 and 2, the whole pattern consists of straight lines, characteristic of a nearly-free electron branch structure. As may be expected, the dynamical effects exhibited by branches 1 and 2 become weaker for materials containing lighter elements.

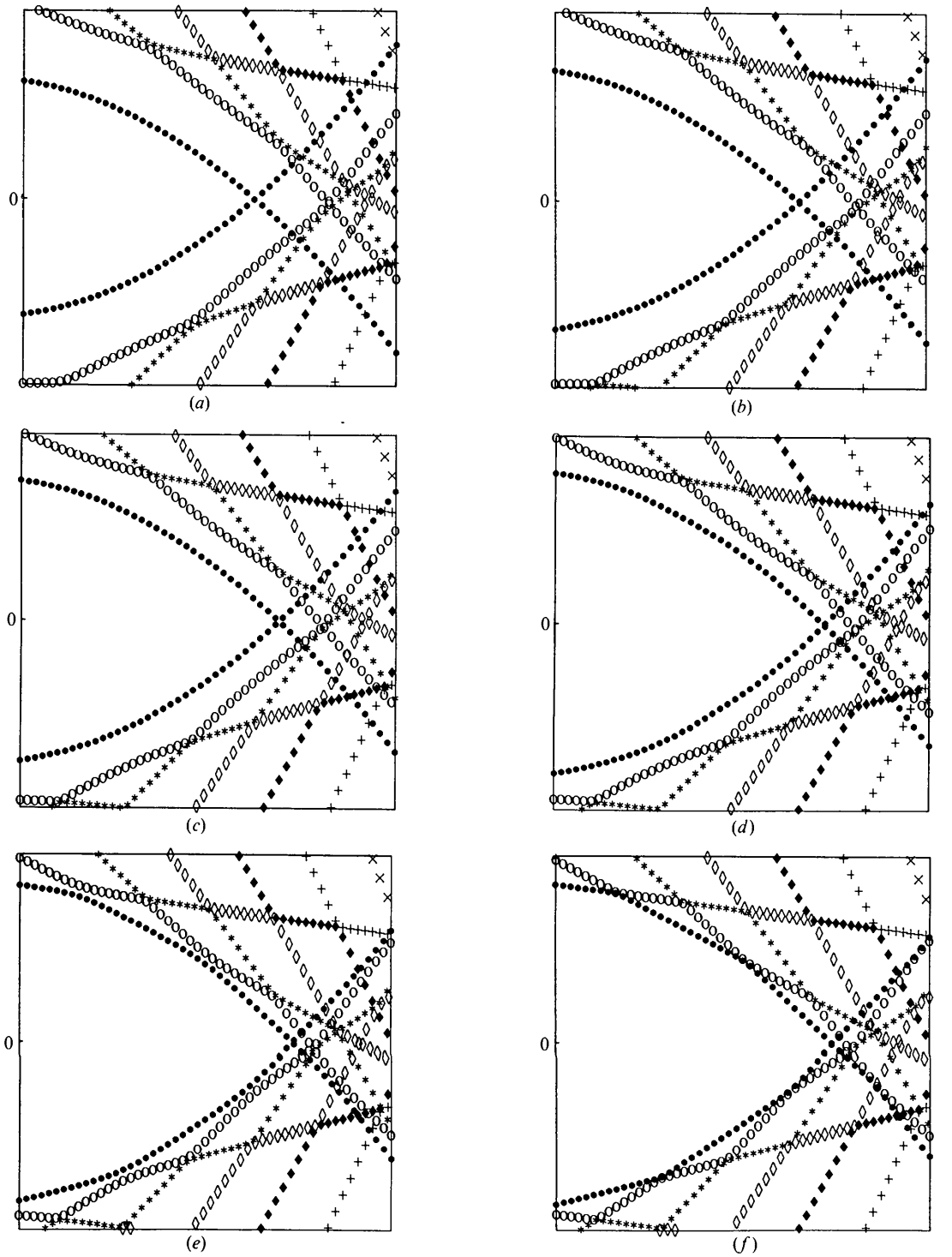

Fig. 7. Series of two-row branch-by-branch simulations of Pt[231] at 200 kV, for various fractions c of the true scattering potential of platinum. (*a*) to (*f*) correspond to $c = 1.0$, 0.8, 0.6, 0.4, 0.2 and 0.01, respectively.

To cement the notion of a dynamically modified Bragg condition, it is instructive to solve (20) for a system in which the scattering potential is systematically switched off. Fig. 7 is a series of two-row branch-by-branch simulations of the [231] pole LACBED patterns, in which the strength of the scattering potential in the $(1\bar{1}1)$ systematic row is artificially set to various fractions of the 'true' potential for platinum. Thus, the first plot (which is the same as Fig. 5) simulates the full platinum potential and the last gives the type of pattern expected from an imagined scatterer with the same structure as platinum but 100 times weaker. The dispersion surface produced by this latter potential is virtually free-electron-like so the lines in the simulation are all in their kinematic positions. The points to observe from Fig. 7 as the potential is increased are as follows.

(i) The position of the branch-1 contribution moves away from the branch-2 envelope and becomes smoother and more parabolic.

(ii) The branch-2 envelope itself changes shape, producing a *different* set of straight-line segments to those seen at 'zero' potential.

(iii) The other lines remain straight and approximately in their kinematic positions. The slight adjustment to this at large potentials is that, close to the left edge of the plots, where the dynamical effects are strongest and where two-row theory is most likely to break down, the lines are shifted slightly. Each then makes a slightly different angle with the vertical than at zero potential.

These observations may also be made by reducing the potential in the full two-dimensional LACBED simulations described in §2. Such calculations confirm that the results we have deduced from perturbation theory are indeed correct. In addition, they suggest that the surface-parallel Bragg lines $(n\bar{n}n)$ also remain in approximately the same place (especially for large n), regardless of the strength of the potential, as would be expected.

5. Discussion and concluding remarks

So far, we have shown that a modified Bragg condition, taking into account dynamical scattering in one dimension (the systematic row direction), can account unequivocally for the positions of deficiency features in bright-field LACBED patterns. The result has been extracted from the mathematical description of the problem using perturbation theory but, as with normal Bragg diffraction, the geometry may also be understood in terms of energy and momentum conservation.

Energy conservation is expressed through (20) – it is the dynamically modified equivalent of the Laue condition $K^2 = (\mathbf{K} \pm \mathbf{H})^2$. We have, of course, only considered elastic scattering of incident electrons. The more interesting conservation is that of momentum, expressed through (15). As already mentioned, both K_x and K_y are good quantum numbers in transmission and must each be conserved to within a reciprocal-lattice vector. K_y is automatically conserved by splitting the problem into systematic rows but, to guarantee K_x conservation, we must introduce the offset Δ. Because of the constraint of conservation of momentum, the loci of plane-wave Bragg conditions must be straight lines. As the dispersion of the branches becomes less parabolic (*i.e.* less like a plane-wave disperson), the lines become less straight. In the extreme limit of a completely dispersionless band (such as $j=1$ in the platinum case above), $\sigma^{(j)}$ does not vary with K_x and the locus is a completely smooth parabola. Although we know that K_x conservation must be obeyed in the formation of the parabola, we would have seen exactly the same shape if it were not obeyed. At a zone axis with nonzero Δ, the parabolas are then the only features from the two rows $G_y = \pm H$ displaying mirror symmetry about $K_y = 0$.

This way of thinking of the problem offers an interesting analogy with RHEED. Since the features in convergent-beam RHEED patterns are so similar to those discussed in this paper, they invite interpretation in terms of energy and momentum conservation *via* a modified Bragg condition. Though the source of the smooth parabolas is well documented [see earlier references, plus Gajdardziska-Josifovska & Cowley (1991)], a complete explanation of all the lines, including the straight ones, has never been given. Though RHEED is a different problem to THEED and additional features (such as absorption) must be included in its analysis, we believe the work presented here gives a solid base from which to start. The existence of straight lines (including the surface-parallel ones) and a definite lack of mirror symmetry about $K_y = 0$ seen in CB-RHEED patterns suggest that the rods are *not* featureless along their length and that sufficient bulk is being penetrated to require at least some degree of K_x conservation. This point and others are addressed and expanded upon in a separate paper (James, Bird & Wright, 1994).

References

Berry, M. V. (1971). *J. Phys. C*, **4**, 697–722.

Bird, D. M. (1987). *Inst. Phys. Conf. Ser.* No. 90, pp. 119–122.

Bird, D. M. (1989). *J. Electron Microsc. Tech.* **13**, 77–97.

Gajdardziska-Josifovska, M. & Cowley, J. M. (1991). *Acta Cryst.* A**47**, 74–82.

Howie, A. (1966). *Philos. Mag.* **14**, 223–237.

James, R., Bird, D. M. & Wright, A. G. (1989). *Inst. Phys. Conf. Ser.* No. 98, pp. 111–114.

James, R., Bird, D. M. & Wright, A. G. (1994). In preparation.

Lehmpfuhl, G. & Dowell, W. C. T. (1986). *Acta Cryst.* A**42**, 569–577.

McRae, E. G. (1979). *Rev. Mod. Phys.* **51**, 541–568.
Marten, H. & Meyer-Ehmsen, G. (1985). *Surf. Sci.* **151**, 570–584.
Peng, L. M., Cowley, J. M. & Yao, N. (1988). *Ultramicroscopy*, **26**, 189–194.
Schiff, L. I. (1968). *Quantum Mechanics*. New York: McGraw-Hill.
Tanaka, M., Saito, R., Ueno, K. & Harada, Y. (1980). *J. Electron Microsc.* **20**, 408–412.
Yao, N. & Cowley, J. M. (1989). *Ultramicroscopy*, **31**, 149–157.

Acta Cryst. (1994). A**50**, 366–375

Projection Description of Cubic Quasiperiodic Crystals with Phason Strains*

By Renhui Wang† and Changsong Qin

Department of Physics, Wuhan University, 430072 *Wuhan, People's Republic of China, and Beijing Laboratory of Electron Microscopy, Chinese Academy of Sciences, PO Box* 2724, 100080 *Beijing, People's Republic of China*

Ganghua Lu

Department of Physics, Wuhan University, 430072 *Wuhan, People's Republic of China, Beijing Laboratory of Electron Microscopy, Chinese Academy of Sciences, PO Box* 2724, 100080 *Beijing, People's Republic of China, and Laboratory of Atomic Imaging of Solids, Institute of Metal Research, Chinese Academy of Sciences*, 110015 *Shenyang, People's Republic of China*

Yongchang Feng

Beijing Laboratory of Electron Microscopy, Chinese Academy of Sciences, PO Box 2724, 10080 *Beijing, People's Republic of China, and Laboratory of Atomic Imaging of Solids, Institute of Metal Research, Chinese Academy of Sciences*, 110015 *Shenyang, People's Republic of China*

and Shengqiu Xu

Department of Physics, Wuhan University, 430072 *Wuhan, People's Republic of China*

(*Received* 10 *July* 1993; *accepted* 1 *November* 1993)

Abstract

A new projection description for a cubic quasiperiodic crystal (CQC), including a projection matrix, diffraction-intensity calculation and a linear phason matrix, has been proposed. The simulated electron diffraction patterns with appropriate phason parameters agree well with the experimental ones obtained for a rapidly solidified $V_6Ni_{16}Si_7$ alloy. The transition from the CQC to its crystalline approximants is treated using the linear-phason-strain concept.

1. Introduction

Since the discovery of the icosahedral quasicrystal (IQC) in Al–Mn alloys (Shechtman, Blech, Gratias & Cahn, 1984), other quasiperiodic crystal (QCs) have been reported, such as the decagonal (Bendersky, 1985), dodecagonal (Ishimasa, Nissen & Fukano, 1985) and octagonal (Wang, Chen & Kuo, 1987) phases. All these quasiperiodic crystals have noncrystallographic point symmetries and can be described with quasiperiodic (QP) tilings projected from a higher-dimensional periodic lattice. However, it is possible to construct QP tilings of crystallographically permissible orientational symmetries. For example, Baranidharan, Balagurusamy, Srinivasan, Gopal & Sasisekharan (1989) constructed a QP tiling with fourfold symmetry and Kulkarni (1989) generated a two-dimensional (2D) QP structure belonging to the 4*mm* point-symmetry group using a modified strip-projection method. This QP structure was interpreted as a superlattice structure of the face-centred-cubic disordered Ni–Mo alloy.

Recently, Janssen (1992) deduced symmetry operations of all possible two- and three-dimensional QP structures of rank 4, 5 or 6, including both noncrystallographic point symmetries such as five-, eight-, ten- and twelvefold symmetries and crystallographic

* This project is supported by the National Natural Science Foundation of China.
† Author for correspondence.